3-D Angle-domain common-image gathers for migration velocity analysis

Biondo Biondi and Thomas Tisserant

– Accepted for publication in *Geophysical Prospecting* **–**

Stanford Exploration Project, Mitchell Bldg., Department of Geophysics,

Stanford University, Stanford, CA 94305-2215

(August 24, 2004)

ABSTRACT

Angle-Domain Common Image Gathers (ADCIGs) are an essential tool for Migration Velocity Analysis (MVA). We present a method for computing ADCIGs in 3-D from the results of wavefield-continuation migration. The proposed methodology can be applied before or after the imaging step in a migration procedure. When computed before imaging, 3-D ADCIGs are functions of the offset ray parameters $\left(p_{x_h}, p_{y_h}\right)$; we derive the geometric relationship that links the offset ray parameters to the aperture angle γ and the reflection azimuth ϕ. When computed after imaging, 3-D ADCIGs are directly produced as functions of γ and ϕ.

The mapping of the offset ray parameters $\left(p_{x_h}, p_{y_h}\right)$ into the angles (γ, ϕ) depends on both the local dips and the local interval velocity; therefore, the transformation of ADCIGs computed before imaging into ADCIGs that are function of the actual angles is difficult in complex structure. In contrast, the computation of ADCIGs after imaging is efficient and accurate even in presence of complex structure and a heterogeneous velocity function. On the other hand, the estimation of the offset ray parameters $\left(p_{x_h}, p_{y_h}\right)$ is less sensitive to velocity errors than the estimation of the angles (γ, ϕ). When ADCIGs that are functions of the offset ray parameters $\left(p_{x_h}, p_{y_h}\right)$ are adequate for

the application of interest (e.g. ray-based tomography), the computation of ADCIGs before imaging might be preferable.

Errors in the migration velocity cause the image point in the angle domain to shift along the normal to the apparent geological dip. By assuming stationary rays (i.e. small velocity errors), we derive a quantitative relationship between this normal shift and the traveltime perturbation caused by velocity errors. This relationship can be directly used in a MVA procedure to invert depth errors measured from ADCIGs into migration velocity updates. In this paper, we use it to derive an approximate 3-D Residual Moveout (RMO) function for measuring inconsistencies between the migrated images at different γ and ϕ. We tested the accuracy of our kinematic analysis on a 3-D synthetic data set with steeply dipping reflectors and a vertically varying propagation velocity. The tests confirm the accuracy of our analysis and illustrate the limitations of the straight-rays approximation underlying our derivation of the 3-D RMO function.

INTRODUCTION

Wavefield-continuation migration methods have the potential of producing high-quality images even when complex overburden severely distorts the wavefield. However, as for all migration methods, the quality of the final image is strongly dependent on the accuracy of the velocity model. In complex area the velocity model is usually estimated in an iterative process called Migration Velocity Analysis (MVA). At each iteration of an MVA process the velocity is updated based on the information extracted from the current migrated image, and, in particular, from the Common Image Gathers (CIGs). The computation of accurate CIG is thus crucial for any MVA method. Most of the current MVA methods for wavefield-continuation migration employ Angle-Domain CIGs (ADCIGs) (Biondi and Sava, 1999; Clapp and Biondi, 2000; Mosher et al., 2001; Liu et al., 2001).

The computation of ADCIGs with wavefield-continuation migration is based on a plane-waves decomposition of the wavefield either before imaging (de Bruin et al., 1990; Mosher et al., 1997; Prucha et al., 1999; Xie and Wu, 2002), or after imaging (Sava and Fomel, 2003; Rickett and Sava, 2002; Biondi and Shan, 2002). The methods previously presented in the literature are limited to the computation of 2-D ADCIGs that are functions of the aperture angle γ only. These methods have been applied to 3-D marine data by assuming zero-azimuth reflections; this assumption is approximately correct for marine data that have been acquired with a narrow-azimuth acquisition geometry.

In this paper we present the computation and the geometric interpretation of full 3-D ADCIGs that decompose the image not only according to the aperture angle γ, but also to the reflection azimuth ϕ. We extend to 3-D both methods for computing ADCIGs: before and after imaging. Our analysis shows that the 2-D equation that relates the in-line offset ray parameter p_{x_h} to the aperture angle γ is also valid in 3-D for zero-azimuth reflections, when used in combination with common-azimuth migration (Biondi and Palacharla, 1996). This result supports the previous use of 2-D ADCIGs computed before imaging for MVA of 3-D marine data (Biondi and Vaillant, 2000; Clapp, 2001; Mosher et al., 2001; Liu et al., 2001). In contrast, the 2-D transformation to angle domain performed after imaging (Sava and Fomel, 2003) is not correct in 3-D, not even in the case of zero-azimuth reflections; its use in presence of cross-line dips leads to the overestimation of the reflection-aperture angle γ. In either case (before or after imaging), when the azimuth of the reflections is not oriented along the in-line direction, we must use the full 3-D methodology to obtain accurate ADCIGs.

The geometrical understanding we developed when generalizing 2-D ADCIGs to 3-D ADCIGs enables us to generalize the analysis of the kinematics of 2-D ADCIGs in the presence of migration-velocity errors that was presented by Biondi and Symes (2004). However their purely ray-theoretical analysis of 2-D ADCIGs cannot be directly extended because in 3-D the source and receiver rays are not guaranteed to be coplanar. Fortunately, a plane-wave interpretation of 3-D ADCIGs overcomes

these difficulties because the two plane waves corresponding to the source and receiver rays define a plane of coplanarity that passes through the angle-domain image point. Once this plane is defined, the 2-D kinematic analysis carries over to 3-D and we can define a quantitative relationship between the reflectors' movement along the apparent geological dip and the traveltime perturbations caused by velocity errors. This relationship can be directly used in a tomographic inversion of 3-D ADCIGs; we use it to define a 3-D RMO function for measuring kinematic errors from 3-D ADCIGs.

ADCIGs have been introduced also for integral migration methods (e.g. Kirchhoff and Generalized Radon Transform); Xu et al. (2001) defined and applied them in 2-D, Brandsberg-Dahl et al. (2003) defined them in 3-D and applied them in 2.5-D, and Brandsberg-Dahl et al. (1999) applied 2-D ADCIGs to MVA. ADCIGs computed by Kirchhoff-like migration share many properties with ADCIGs computed by wavefield-continuation migration. However, in complex media, the two types of ADCIG have subtle kinematic differences, as clearly demonstrated by Stolk and Symes (2004). A thorough comparison of these two types of ADCIG would be of theoretical and practical value, but we consider it beyond the scope of this paper.

ANGLE-DOMAIN COMMON IMAGE GATHERS BEFORE IMAGING

This paper presents two methods for computing 3-D ADCIGs in conjunction with wavefield-continuation migration. Both methods rely on a decomposition of the wavefield into plane-wave components; this decomposition is performed by slant stacks (Schultz and Claerbout, 1978) along the subsurface offset axes. The two methods differ in the stage of the migration process during which the plane-wave decomposition is performed (before imaging or after imaging), but in both cases the plane-wave decomposition links the ray-theoretical and the plane-wave interpretation of ADCIGs that we use in this paper. We equate the propagation direction of plane waves with the propagation direction of

specular rays, and thus we implicitly make a stationary-phase approximation that assumes that the seismic events are not dispersive; that is, that wavefronts are locally planar and coherent for all frequencies. This assumption is not strictly necessary because our analysis is valid for each frequency component, but nonetheless we believe that the advantages in simplicity are worthwhile the apparent loss of generality.

We start by presenting the method based on an angle decomposition before imaging (de Bruin et al., 1990; Prucha et al., 1999) because it has the most direct physical interpretation. The physical interpretation of the ADCIGs computed after imaging (Sava and Fomel, 2003; Rickett and Sava, 2002; Biondi and Shan, 2002) follows directly from the interpretation of the ADCIGs computed before imaging.

A 3-D prestack data set can be decomposed according to the offset ray parameters (p_{x_h}, p_{y_h}) by applying slant stacks along the offset axes. These slant stacks produce plane-wave components called offset plane waves. If the velocity function is horizontally invariant, each offset plane wave can be accurately propagated and imaged independently from the others. Each prestack partial image produced by this procedure corresponds to one offset ray parameter, and thus ADCIG functions of the offset ray parameters $[\mathrm{ADCIG}(p_{x_h}, p_{y_h})]$ can be extracted from the whole prestack image cube. The offset ray parameters measured at the surface are functions of the surface take-off angles of the source and receiver rays, and are obviously linked with the reflection opening angle γ and the reflection azimuth ϕ.

Ottolini and Claerbout (1984) presented a procedure for obtaining angle-dependent images based on the slant-stack of 2-D CMP gathers at the surface and on the propagation of offset plane waves. Mosher et al. (1997) generalized the 2-D procedure to 3-D marine data and derived a more accurate downward-continuation method for the offset plane waves. However, there is a limit on the accuracy

of a migration based on an offset plane-wave decomposition at the surface. When the velocity function is laterally varying, the source and receiver wavefields are refracted differently, according to the local velocities. Consequently, the independent propagation of each offset plane wave is inaccurate when strong lateral velocity variations occur. In these situations, the idea of decomposing the wavefield into offset plane waves is still useful, but it must be generalized; the prestack wavefield must be slant-stacked recurrently at each depth level, instead of only once at the surface.

When source-receiver migration (i.e. survey sinking) is applied, the whole prestack wavefield is obtained at every depth level as the result of recursively downward continuing the recorded data using the Double Square Root (DSR) operator (Claerbout, 1985). Therefore, once we have introduced the concept of decomposing the prestack wavefield at depth, the derivation of the procedure for computing ADCIGs before imaging using source-receiver downward continuation is straightforward (Prucha et al., 1999).

In conventional source-receiver migration the image is then obtained by extracting the values of the wavefield at zero time ($t = 0$). The migration process can be schematically represented as follows:

$$P(\omega, \mathbf{m}, \mathbf{h}; z = 0) \quad \stackrel{\text{DSR}}{\Longrightarrow} \quad P(\omega, \mathbf{m}, \mathbf{h}; z) \tag{1}$$

$$P(\omega, \mathbf{m}, \mathbf{h}; z) \quad \stackrel{Imaging}{\Longrightarrow} \quad P(t = 0, \mathbf{m}, \mathbf{h}; z), \tag{2}$$

where $P(\omega, \mathbf{m}, \mathbf{h}; z)$ is the wavefield at the temporal frequency ω, the midpoint $\mathbf{m}$, the offset $\mathbf{h}$, and at depth z.

To compute ADCIGs, we need to introduce a slant-stack transformation between downward continuation [step (1)] and imaging [step (2)]. The results of slant stacks are functions of the offset ray parameter $\mathbf{p_h}$ and the intercept time τ. The image is then obtained by extracting the values of the wavefield at zero intercept time; i.e. $\tau = 0$. The migration process used to produce ADCIGs can be

schematically represented as follows:

$$P(\omega, \mathbf{m}, \mathbf{h}; z = 0) \quad \overset{\text{DSR}}{\Longrightarrow} \quad P(\omega, \mathbf{m}, \mathbf{h}; z) \tag{3}$$

$$P(\omega, \mathbf{m}, \mathbf{h}; z) \quad \overset{\textit{Slant stack}}{\Longrightarrow} \quad P(\tau, \mathbf{m}, \mathbf{p_h}; z) \tag{4}$$

$$P(\tau, \mathbf{m}, \mathbf{p_h}; z) \quad \overset{\textit{Imaging}}{\Longrightarrow} \quad P(\tau = 0, \mathbf{m}, \mathbf{p_h}; z). \tag{5}$$

Figure 1 illustrates the subsequent stages of the process represented in (3–5). The synthetic data set imaged to create this figure was modeled assuming two reflectors (one dipping and one flat) immersed in a constant-velocity medium. The downward-continuation process [step (1) or step (3)] focuses the wavefield toward zero offset; if the continuation velocity is correct, a migrated image can be obtained by extracting the value of the wavefield at zero offset and zero time. Figure 1a shows the zero-offset section of the downward-continued wavefield at the depth of the flat reflectors; that is, at $z = 700$ meters. As expected, the flat reflector is well imaged at zero time. Figure 1b shows the wavefield at the same depth as in Figure 1a, but as a function of offset and at fixed midpoint ($x_m = 1,410$ meters). The flat reflector is well focused at zero offset and zero time, whereas the energy corresponding to the dipping reflector has already been defocused and thus it appears as a "time-reversed" hyperbola at negative times. The wavefield shown in Figure 1b is decomposed into plane waves by performing slant stacks for each midpoint location [step (4)], and the results of these slant stacks are imaged at zero time [step (5)]. The downward-continuation, slant stacks, and imaging steps are repeated for all depth levels. Figure 1c shows the ADCIG at $x_m = 1,410$ meters, for all depths. Both reflectors are imaged as flat events in the ADCIGs, because at each depth, slant stacks transform band-limited impulses located at zero offset (like the one shown in Figure 1b) into flat events.

Computing ADCIGs before imaging is more difficult when using shot-profile migration than when using source-receiver migration, because the prestack wavefield at depth is not easily available

as a function of the subsurface offset. In theory, it could be computed by appropriate correlations (or deconvolutions) of the source and receiver wavefields (de Bruin, 1992). This procedure generates ADCIGs equivalent to those obtained by source-receiver migration, as it can be demonstrated by a generalization of the equivalence principle for the prestack images demonstrated by Wapenaar and Berkhout (1987) and Biondi (2003). The computation of the ADCIGs before imaging for shot-profile migration is computationally demanding, because it requires either decomposing the wavefield for each shot independently and accumulating the prestack images for all shots (computationally inefficient), or, accumulating the contributions of each shot to the whole prestack wavefield before decomposing it (storage and I/O inefficient). Therefore, ADCIGs are rarely computed before imaging when using shot-profile migration. In the next section we will see how computing ADCIGs after imaging addresses this problem.

Geometric interpretation of 3-D ADCIG$\left(p_{x_h}, p_{y_h}\right)$

Regardless of whether they have been computed using source-receiver migration or shot-profile migration, ADCIGs computed before imaging have the same geometrical interpretation. Strictly speaking, they are functions of the offset ray parameters (p_{x_h}, p_{y_h}) and not of the reflection opening angle γ and the reflection azimuth ϕ. However, the offset ray parameters (p_{x_h}, p_{y_h}) are easily related to γ and ϕ by simple trigonometric relationships. We now derive these relationships, starting from the simpler 2-D case. The understanding gained from the 2-D analysis will help the analysis of the more complex 3-D case.

The schematic in Figure 2 defines the angles relevant to 2-D ADCIGs: the reflection opening angle γ and the geological dip angle α_x, which is defined as the angle formed by the vertical direction and the normal to the apparent geological dip **n**, both oriented in the upward direction. The box in

Figure 2 signifies that for the purpose of our discussion the geometric relationships are local around the imaging point $\bar{\mathbf{I}}$.

The opening angle and the dip angle are related to the source and receiver rays (plane waves) propagation angles (β_s, β_r) by the following simple relationships:

$$\gamma = \frac{\beta_r - \beta_s}{2}, \quad \text{and} \quad \alpha_x = \frac{\beta_s + \beta_r}{2}. \tag{6}$$

The source ray parameter p_{x_s} and the receiver ray parameter p_{x_g} are related to the midpoint ray parameters p_{x_m} and offset ray parameter p_{x_h} by the following relationships:

$$p_{x_m} = p_{x_g} + p_{x_s}, \quad \text{and} \quad p_{x_h} = p_{x_g} - p_{x_h}. \tag{7}$$

In 2-D the source and receiver ray parameters (p_{x_s}, p_{x_g}) are functions of the source and receiver ray propagation angles (β_s, β_r) and of the velocity at the reflector $v(z,x)$ as follows:

$$p_{x_s} = \frac{\sin\beta_s}{v(z,x)} \quad \text{and} \quad p_{x_g} = \frac{\sin\beta_r}{v(z,x)}. \tag{8}$$

Substituting the relationships in (8) into equation (7), then using the angular relationship expressed in equation (6) and applying fundamental trigonometric identities, we obtain the desired relationship:

$$p_{x_h} = \frac{\sin\beta_r - \sin\beta_s}{v(z,x)} = \frac{2\sin\left(\frac{\beta_r-\beta_s}{2}\right)\cos\left(\frac{\beta_r+\beta_s}{2}\right)}{v(z,x)} = \frac{2\sin\gamma\cos\alpha_x}{v(z,x)}, \tag{9}$$

which directly links the offset ray parameter p_{x_h} to the reflection opening angle γ.

The relationship in equation (9) is also valid in 3-D when the reflection azimuth ϕ is equal to zero. But in the general 3-D case we need to add another relationship linking the cross-line offset ray parameter p_{y_h} to p_{x_h} and the angles γ and ϕ at the reflection point. To derive this relationship, we impose the constraint that the source and the receiver rays must become coplanar before meeting at the reflection point. We will thus refer to this relationship as the coplanarity condition.

The coplanarity of the two rays also simplifies the 3-D geometry of ADCIGs and enables us to generalize the 2-D geometric interpretation in a straightforward manner. The schematic in Figure 3 is the 3-D generalization of the 2-D schematic shown in Figure 2. The plane that is shared by the two rays in 3-D corresponds to the vertical plane in 2-D. As for Figure 2, all the geometric relationships represented in Figure 3 are local in a neighborhood of the image point $\bar{\mathbf{I}}$. This locality implies that the source and receiver rays (plane waves) need to satisfy the coplanarity condition only at the image point, not during propagation in the overburden.

We define the reflection azimuth angle ϕ as the angle formed by the in-line axis x with the line defined by the intersection of the plane of coplanarity with a constant depth plane. After rotation by ϕ, the horizontal coordinates x and y become x' and y', respectively. Once rotated by ϕ, the plane of coplanarity is tilted with respect to the vertical by the cross-line dip angle $\alpha_{y'}$. All the angles in Figure 2 that are formed between the ray (plane wave) directions and the true vertical axis z ($\beta_{s'}$, $\beta_{r'}$, and $\alpha_{x'}$) are now relative to the tilted vertical axis z'; these angles have the same meaning on the tilted plane as they have on the vertical plane in 2-D. Furthermore, the horizontal ray parameters $(\mathbf{p}_{\mathbf{s}'}, \mathbf{p}_{\mathbf{g}'})$ are not affected by the tilt, since they depend on the angles formed by the rays with the x axis. In contrast, the angles $\beta_{s'}$, $\beta_{r'}$, $\alpha_{x'}$, and $\alpha_{y'}$ are affected by the rotation of the horizontal axes by ϕ; we include the prime in the notation to indicate the angles after rotation.

Imposing the coplanarity of the source and receiver rays along a plane rotated by ϕ with respect to the original coordinate system provides us with the needed relationship that constraints the cross-line offset ray parameter $p_{y'_h}$. For the azimuth of the plane of coplanarity to be ϕ, the "rotated" source and receiver ray-parameters $p_{x'_s}, p_{y'_s}, p_{x'_g}, p_{y'_g}$ must be related by the following expression:

$$\left(p_{y'_g} - p_{y'_s}\right) = \left(p_{y'_g} + p_{y'_s}\right) \frac{\sqrt{\frac{1}{v^2(\mathbf{g}',z)} - p_{x'_g}^2} - \sqrt{\frac{1}{v^2(\mathbf{s}',z)} - p_{x'_s}^2}}{\sqrt{\frac{1}{v^2(\mathbf{g}',z)} - p_{x'_g}^2} + \sqrt{\frac{1}{v^2(\mathbf{s}',z)} - p_{x'_s}^2}}. \tag{10}$$

This relationship was derived by Biondi and Palacharla (1996) to define common-azimuth migra-

tion. It can be derived either by using stationary-phase, or by geometric considerations.

So far we have interpreted the coplanarity condition in terms of source and receiver rays, but it has a similar interpretation in terms of plane waves. The phase vectors of two arbitrary plane waves are coplanar by construction, since they meet at the origin. The tilt angle $\alpha_{y'}$ and the azimuth ϕ of the plane of coplanarity for the incident and the reflected plane waves are implicitly determined by the coplanarity condition expressed in equation (10). The cross-correlation of the two plane waves does not define an imaging point but an imaging line that is orthogonal to the plane of coplanarity. The tilted plane shown in Figure 3 is an arbitrary plane parallel to the plane of coplanarity and the imaging point $\bar{\mathbf{I}}$ is the intersection of the imaging line with this plane. The source and receiver rays are defined as the lines parallel to the phase vectors of the corresponding plane waves and passing through the imaging point $\bar{\mathbf{I}}$.

Using the relationships among the in-line ray parameters expressed in equations (7) (and their analogues along the cross-line direction y), and equations (8), and after applying trigonometric identities, we can rewrite equation (10) as a function of the local velocity $v\left(z',x',y'\right)$ and the angles $\alpha_{x'}$,$\alpha_{x'}$, γ and ϕ as follows:

$$p_{y'_h} = \frac{\sin\alpha_{y'}\left(\cos\beta_r - \cos\beta_s\right)}{v\left(z',x',y'\right)} = -\frac{2\,\sin\alpha_{y'}\sin\gamma\,\sin\alpha_{x'}}{v\left(z',x',y'\right)}. \tag{11}$$

The in-line offset ray parameter from equation (9) can be rotated by the azimuth ϕ to give the following expression:

$$p_{x'_h} = \frac{2\,\sin\gamma\cos\alpha_{x'}}{v\left(z',x',y'\right)}, \tag{12}$$

which together with equation (11), can be used to map the image from the offset ray parameter domain $\left(p_{x_h}, p_{y_h}\right)$ into the angle domain (γ,ϕ).

This mapping of the ray parameters into angles depends on both the local velocity and the geological dips. When the spatial velocity variations are significant and the geological structure is complex,

unraveling this dependence might be a challenge because of the well known difficulties in reliably measuring rapidly changing local dips. For some applications this dependency does not cause difficulties. For example, in a ray-based MVA (Clapp and Biondi, 2000), there is no need to perform the mapping from ray parameters to angles, since ray parameters are adequate initial conditions for ray tracing. For other applications, the reflection angles are needed, and thus the mapping must be performed. When this mapping is difficult, it might be convenient to use the ADCIGs computed after imaging, which are presented in the next section. This kind of ADCIG circumvents the need to estimate local dips by transforming the image directly into angles.

ANGLE-DOMAIN COMMON IMAGE GATHERS AFTER IMAGING – ADCIG(γ, ϕ)

The computation of ADCIGs before imaging has a straightforward physical interpretation, and thus it was the first methodology to be developed for both and shot-profile migration (de Bruin et al., 1990) and source-receiver migration (Prucha et al., 1999). However, as we have discussed in the previous section, the computation of ADCIGs before imaging with shot-profile migration can be either computationally or I/O demanding. Sava and Fomel (2003) recognized that for source-receiver migration, the plane-wave decomposition can be performed after applying the imaging condition, as well as before. Rickett and Sava (2002) applied this insight to compute 2-D ADCIGs after shot-profile downward continuation. Their method is based on the generalization of the conventional imaging condition for shot-profile migration that we summarize in the next paragraph. When using this imaging condition we compute a prestack image function of the subsurface half offset $\mathbf{h}$, as well as of depth z and the midpoint $\mathbf{m}$.

If $P_z^s(\omega, x, y; \mathbf{s}_i)$ and $P_z^g(\omega, x, y; \mathbf{s}_i)$ are respectively the source wavefield and the recorded wavefield downward-continued to depth z for the i-th source location $\mathbf{s}_i$, as functions of the subsurface

horizontal coordinates (x, y), the image is formed by first cross-correlating the two wavefields along the time axis (multiplication by the complex conjugate in the frequency domain) and then evaluating the correlation at zero time (summation over frequencies) as following:

$$I(\mathbf{m}, \mathbf{h}; z) = \sum_i \sum_\omega P_z^g(\omega, x + x_h, y + y_h; \mathbf{s}_i) \overline{P_z^s(\omega, x - x_h, y - y_h; \mathbf{s}_i)}. \tag{13}$$

The physical interpretation of the subsurface offsets from equation (13) is not immediate. However, it can be demonstrated (Wapenaar and Berkhout, 1987; Biondi, 2003) that the prestack image $I(\mathbf{m}, \mathbf{h}; z)$ obtained by equation (13) is equivalent to the image obtained by source-receiver migration applying the procedure outlined in equations (1) and (2). The subsurface offsets can thus be equated to the data offset of the recorded data datumed at depth.

The computation of the ADCIGs after imaging is based on a plane-wave decomposition of the prestack image $I(\mathbf{m}, \mathbf{h}; z)$ – which is obtained by either source-receiver migration or shot-profile migration – by applying slant-stacks along the offset axes, similarly to the computation before imaging that we discussed in the previous section. The only difference between the two methods (before and after imaging) is that the dips along the offset axes are affected by the transformation from time to depth that is implicit in the imaging step. Therefore, the offset-dip parameters are linked to the reflection opening angle γ and azimuth ϕ differently than in the previous case. We will now derive and discuss the analytical relationships between reflection angles and offset dips after imaging. We will start with the simpler 2-D case (Sava and Fomel, 2003), and then address the general 3-D case (Biondi et al., 2003).

The application of the imaging condition transforms a wavefield propagating in time into an image cube that is a function of depth. The transformation from time to depth depends on the local dips in the wavefield and the local propagation velocity. In the frequency-wavenumber domain this transformation is represented by the DSR operator, which in 2-D can be expressed as a function of

the angles β_s and β_r as follows:

$$k_z = -\frac{\omega}{v(z,x)}(\cos\beta_r + \cos\beta_s). \tag{14}$$

Recalling the relationship between the in-line offset wavenumber k_{x_h} and the in-line offset ray parameter p_{x_h}:

$$k_{x_h} = p_{x_h}\omega, \tag{15}$$

and substituting both equation (14) and equation (9) in equation (15), we obtain the following relationship:

$$k_{x_h} = -p_{x_h}\frac{k_z v(z,x)}{\cos\beta_r + \cos\beta_s} = -\frac{2\sin\gamma\cos\alpha_x}{v(z,x)}\frac{k_z v(z,x)}{2\cos\gamma\cos\alpha_x} = -k_z\tan\gamma. \tag{16}$$

This relationship directly links the dips in the depth-offset domain $\left(k_{x_h}/k_z\right)$ to the aperture angle $(\tan\gamma)$.

Figure 4 illustrates the computation of 2-D ADCIGs after imaging with a synthetic example. It is analogous to Figure 1, which illustrates the computation of 2-D ADCIGs before imaging. Figure 4a shows a vertical section of the prestack image taken at constant midpoint. We will refer to this kind of section as an Offset Domain Common Image Gather (ODCIG). This ODCIG was obtained with the correct velocity, and the energy is well focused at zero offset for both the dipping and the flat reflectors. Slant stacks transform the impulses at zero offset into flat events in the angle domain (Figure 4b).

To generalize the 2-D offset-to-angle transformation to 3-D, we use the coplanarity condition and the geometrical model shown in Figure 3. In this context, the 2-D DSR expressed in equation (14) describes upward-propagating waves on the tilted plane shown in Figure 3, instead of the vertical plane shown in Figure 2. Consequently, the vertical wavenumber in equation (14) is now the vertical wavenumber along the tilted vertical axis $k_{z'}$, and not the vertical wavenumber along the "true" vertical direction. This distinction is irrelevant in the case of ADCIGs computed before imaging because

the computation is performed at each depth level independently, but it is required in this case because the plane-wave decomposition is performed in the depth domain.

If $\delta_{s'}$ and $\delta_{r'}$ are the angles that the source and receiver rays (plane waves) form with the "true" vertical direction (as indicated in Figure 3), simple trigonometry relates these angles to $\beta_{s'}$ and $\beta_{r'}$ through the tilt angle $\alpha_{y'}$ as follows: $\cos\delta_{s'} = \cos\beta_{s'}\cos\alpha_{y'}$, and $\cos\delta_{r'} = \cos\beta_{r'}\cos\alpha_{y'}$. The vertical wavenumber $k_{z'}$ is thus related to the vertical wavenumber k_z as follows: $k_{z'} = k_z/\cos\alpha_{y'} = \sqrt{k_z^2 + k_{y'}^2}$. Substituting this relationship into equation (16) leads to its 3-D equivalent:

$$k_{x'_h} = -k_{z'}\tan\gamma = -\sqrt{k_z^2 + k_{y'}^2}\tan\gamma. \tag{17}$$

This 3-D expression is not independent of the geological dips as was its 2-D equivalent [equation (16)]. In the presence of significant cross-line dips, it is thus important to use the correct 3-D expression in place of the approximate 2-D one. Figures 5–6 illustrate with a data example the effects of the cross-line dip correction in equation (17).

When deriving the after-imaging equivalent of equation (11), we need to take into account that $\alpha_{x'}$ is also measured along the tilted axis and thus that $\tan\alpha_{x'} = -k_{x'}/k_{z'}$. Using equation (11) and equation (17) we derive the following relationship, which expresses $k_{y'_h}$ as a function of the other wavenumbers in the image:

$$k_{y'_h} = -k_{y'}\tan\gamma\tan\alpha_{x'} = -\frac{k_{y'}k_{x'_h}k_{x'}}{{k_{z'}}^2} = -\frac{k_{y'}k_{x'_h}k_{x'}}{k_z^2 + k_{y'}^2}. \tag{18}$$

The combination of equation (17) and equation (18) enables the computation of 3-D ADCIGs after imaging; using these two relationships, we can map the prestack image from the offset domain (x_h, y_h) to the angle domain (γ, ϕ). Notice that the reflection azimuth ϕ is implicitly included in these equations since, all the wavenumbers, with the exception of k_z, are dependent on ϕ. Therefore, during computations the wavenumbers need to be properly transformed by rotating the horizontal axes by the azimuth angle ϕ.

In contrast with the transformation described by equations (9) and (11), the transformation described by equations (17-18) is independent of the local velocity $v(z,x,y)$. Therefore there is no need to estimate the geological dips locally, but only globally. This estimate can be performed accurately and efficiently in the wavenumber domain. However, it is important to notice that the absence of the local velocity $v(z,x,y)$ from the expressions used to compute ADCIGs after imaging does not make the result independent from the local migration velocity. This dependence is indirect through the vertical wavenumber k_z; or, in other words, the estimates of γ and ϕ depend on the apparent vertical wavelength of the imaged reflectors. Therefore, the advantages derived from the absence of $v(z,x,y)$ in equations (17-18) are purely computational. The sensitivity of the estimates of γ and ϕ on the accuracy of the local velocity $v(z,x,y)$ is the same, regardless of whether γ and ϕ are estimated indirectly through p_{x_h} and p_{y_h} by using equations (9) and (11), or directly by using equations (17-18). This concept is well illustrated by the example shown in the last section (Figures 11–12).

There are two alternative computational algorithms to numerically perform the transformation described by equations (17-18); they differ in whether the computations are performed with the offset axes in the space or wavenumber domain. In either case, it is computationally advantageous to perform the computation in the wavenumber domain $\left(k_z, k_x, k_y\right)$ for the physical coordinates, because of the dependence of the mapping on the geological dips. If the ADCIGs are computed for many values of γ and ϕ, it is less expensive to perform the computation in the offset-wavenumber domain by a 3-D generalization of the 2-D radial-trace transform used by Ottolini and Claerbout (1984) and Sava and Fomel (2003). However, this approach can generate artifacts, because the subsurface-offset axes are usually short, and the Fourier transforms have circular boundary conditions. The computation of the slant stack by integration in the offset-space domain avoids these artifacts and can be preferable when high-quality gathers are needed.

Examples of 3-D ADCIGs

This section presents several examples of 3-D ADCIGs. The first example is taken from the SEG-EAGE salt data set (Aminzadeh et al., 1996). It illustrates the error introduced when the approximate 2-D relationship [equation (16)] is used instead of the correct 3-D one [equation (17)] to estimate the aperture angle γ in presence of significant geological dips.

Figure 5 shows a depth slice (z=580 meters) of the migrated image of the SEG-EAGE salt data set. The crosshair is centered at a horizontal location where the top of the salt dips at approximately 50 degrees in the cross-line direction and is flat along the in-line direction. Figure 6 shows the ADCIGs computed at the location marked by the crosshair. Figure 6a was computed using the 2-D relationship [equation (16)], whereas Figure 6b was computed using the 3-D relationship [equation (17)]. The aperture angle is overestimated in the gather on the left (apparent maximum aperture is about 60 degrees), and correctly estimated in the gather on the right (apparent maximum aperture is about 48 degrees). This error is consistent with the factor $\cos\alpha_{y'}$ that is neglected in the 2-D case. Notice that the bottom of the salt reflection ($z \simeq$ 2,100 meters) is unchanged, because it is flat.

In 3-D, ADCIGs are five-dimensional objects, and thus it can be challenging to gain an intuitive understanding of their behavior. The next set of figures shows 2-D slices of the 5-D space generated by computing 3-D ADCIGs from the migrated cube obtained from a simple synthetic data set. The data set contains 5 dipping planes, dipping at 0°, 15°, 30°, 45° and 60° toward increasing x and y. The azimuth of the planes is 45 degrees with respect to the direction of the acquisition. The velocity is $V(z) = (1,500 + .5z)$ m/s, which roughly corresponds to typical gradients found in the Gulf of Mexico. The acquisition geometry had a single azimuth oriented along the x axis, and the maximum source-receiver offset was 3,000 meters. Figure 7 shows the geometry of the reflectors. The data were imaged with a full source-receiver 3-D prestack migration.

Because of the velocity gradient and the oblique azimuthal orientation, the azimuths of the reflections are not equal to the azimuth of the acquisition ($\phi = 0$). The reflection azimuths are within the range of $0^\circ \leq \phi \leq 15^\circ$ and depend on the reflector dip and on the aperture angle γ. The steeper the reflector dip and the wider the aperture angle are, the larger the azimuth rotation is at the reflection point.

All the following figures show slices of the ADCIGs at one fixed horizontal location with $x = y =$ 450 meters; that is, they show slices through the 3-D image cube described as ADCIG(z, γ, ϕ). The most familiar of these slices display the image as a function of the depth (z) and the aperture angle (γ). Figure 8 shows two of these ADCIGs, for two different reflection azimuths: $\phi = 10$ degrees (panel a) and $\phi = 15$ degrees (panel b). The reflections from the deepest – and steepest – reflector ($z \simeq 1{,}430$ meters) are well focused within the range delimited by these two azimuths. In contrast, the reflections from the other two reflectors (dipping at 30 and 45 degrees), are not well focused at these azimuths, and thus they frown downward even if the migration velocity is correct. The frowning is particularly evident in the slice corresponding to the largest reflection azimuth; that is, in panel b)

Figure 9 shows a slice taken at the constant depth of $z = 1{,}430$ meters; this depth corresponds to the deepest reflector. The reflection amplitudes are thus shown as functions of both the aperture angle (γ) and the reflection azimuth (ϕ). Because of the poor azimuthal resolution close to normal incidence, the azimuthal range is wide for small γ; it narrows around $\phi = 15$ degrees as γ increases. The narrowing of the azimuthal range is caused by the uneven and partial coverage of the reflection azimuths afforded by common-azimuth data. Common-azimuth data "illuminates" all the reflection azimuths for narrow aperture angles, but "illuminates" only a narrow range of reflection azimuths at wide aperture angles.

The decreasing of azimuthal coverage is clearly demonstrated in Figure 10. The three panels in

Figure 10 display the image as a function of depth (z) and reflection azimuth (ϕ), and at constant aperture angle. The aperture angles are: a) γ=4 degrees, b) γ=20 degrees, and c) γ=30 degrees. The curvature of the reflectors as a function of the azimuth increases with increasing aperture angle, indicating that the azimuthal coverage of the data decreases as as the aperture angle widens.

ANGLE-DOMAIN COMMON IMAGE GATHERS AND VELOCITY

Migration Velocity Analysis (MVA) is one of the most important applications of ADCIGs, and the main focus of this paper. MVA from ADCIGs computed using wavefield-continuation migration is conceptually analogous to MVA from conventional offset-domain CIGs obtained by Kirchhoff migration. The ADCIGs are analyzed for departure from flatness, usually by applying some kind of Residual Moveout (RMO) analysis. The RMO analysis provides measurements of depth errors that are first transformed into traveltime perturbations and finally inverted into velocity perturbations by a ray-based tomographic inversion. This process is repeated several times in order to converge to a satisfactory result.

In this section we analyze the kinematic properties of 3-D ADCIGs when the migration velocity is not correct. First, we qualitatively analyze the sensitivity of the estimation of the angles (γ,ϕ) to velocity errors. Second, we develop a quantitative relationship between depth errors in ADCIGs and traveltime perturbations caused by velocity errors. Third, we present a 3-D RMO function for measuring the depth errors in ADCIGs. Finally, we compare the imaging-point shifts predicted by our results with the actual images produced from a synthetic data set migrated with the wrong velocity.

Sensitivity of the estimation of (γ, ϕ) to velocity errors

We start with a simple 2-D qualitative analysis of the effects of velocity errors on both kinds of ADCIGs that we presented; that is, ADCIGs computed before imaging and ADCIGs computed after imaging. This first step illustrates the sensitivity of the estimation of the angles (γ, ϕ) to velocity errors. Figure 11 shows the effects of velocity errors on ADCIGs computed before imaging. It shows the same panels as Figure 1 [i.e. wavefield at zero-offset (a), wavefield at fixed midpoint (b), and ADCIG (c)], but when the migration velocity is 10% higher than the correct one. At the correct depth of the flat reflector ($z = 700$ meters), the energy for both reflectors has started defocusing and it forms time-reversed hyperbolas. Most of the energy for the flat reflector has not reached the zero-time line yet, causing the flat reflector to be imaged deeper than the correct depth. In the ADCIG both events frown downward, and thus they indicate too high of a migration velocity. The residual moveout caused by velocity errors in ADCIGs is thus qualitatively similar to the moveout observed in conventional surface-offset CIGs computed by Kirchhoff migration. If the velocity function is too low the reflections will smile upward; if the velocity function is too high the reflections will frown downward.

Figure 12 shows the effects of velocity errors on ADCIGs computed after imaging. It shows the same panels as Figure 4 [i.e. ODCIG (a), and ADCIG (b)], but when the migration velocity is 10% higher than the correct one. The energy is defocused in the ODCIGs and the events have a hyperbolic moveout (Figure 12a); the apexes of the hyperbolas are deeper than the reflectors' true depths. Slant stacks transform the hyperbolas into frowns (Figure 12b) that are similar to the frowns shown in Figure 11c. However, there is a subtle but important difference between the two cases. The p_{x_h} range does not change between the ADCIG shown in Figure 1c and the one shown in Figure 11c, whereas the γ range increases when the velocity is too high (Figure 12b). This increase is due to the increase

in the apparent vertical wavelength in the image, which correspondingly causes a decrease of k_z in equation (16). Or, from a different viewpoint, if we were to use equation (9) to map p_{x_h} into γ, the mapping would be affected by both the increase in $v(z,x)$ and the increase in apparent geological dip α_x – and the corresponding decrease in $\cos\alpha_x$. This simple example illustrates the fact that the estimates of γ and ϕ are similarly sensitive to the accuracy of the local velocity $v(z,x,y)$, regardless of whether ADCIGs are computed before or after imaging.

Kinematic properties of 3-D ADCIGs

Biondi and Symes (2004) analyze in detail the kinematic properties of 2-D ADCIGs when the migration velocity is not correct. Their analysis can be extended to 3-D by following the same geometrical considerations we used in the previous sections to generalize ADCIGs from 2-D to 3-D (Figure 3). However, there is an important conceptual difference between the 2-D case and the 3-D case.

To quantify the reflector movement as a function of the velocity errors, Biondi and Symes (2004) relied on the fact that the source and receiver rays cross even when the data are migrated with the wrong velocity; below the imaging point in case of too low migration velocity and above the imaging point in the opposite case. In 3-D, this assumption is easily violated because the coplanarity of the source and receiver rays is assured only when the velocity is correct and the rays meet at the reflection point. In the general case, when the velocity is inaccurate, it may happen that the two rays do not meet and, consequently, cannot be coplanar. Fortunately, the plane-wave interpretation is still valid and the plane of coplanarity of Figure 13 is determined by the coplanarity condition expressed in equation (10) applied to the phase vectors of the incident and reflected plane waves, or, alternatively by the coplanarity condition expressed in equation (18) applied to the offset dips present in the prestack image. Once this plane is defined, the geometrical relations between the objects (rays

and imaging points) that lie on the vertical plane in 2-D (Biondi and Symes, 2004), directly apply to 3-D on the tilted plane of coplanarity, as it is schematically represented in Figure 13. The source and receiver rays are respectively the projections of the phase vectors of the incident and reflected plane waves on the plane of coplanarity. The offset-domain image point, $\mathbf{I}_{\mathbf{x_h}}$, is at the midpoint between $\mathbf{S}_{\mathbf{x_h}}$ and $\mathbf{R}_{\mathbf{x_h}}$, which are defined by the intersection of the source and receiver rays with a horizontal plane. The depth of this plane is such that the total traveltime along the two rays is equal to the traveltime of the event being imaged.

The source and receiver plane waves constructively interfere along an imaging line; the angle-domain image point, $\mathbf{I}_\gamma$, is defined as the intersection of this imaging line with the tilted plane of coplanarity. Since both the angle-domain image point, $\mathbf{I}_\gamma$, and the offset-domain image point, $\mathbf{I}_{\mathbf{x_h}}$, lie on the tilted plane, the 2-D results directly translate into the following 3-D results:

1. The transformation to the angle domain shifts the image point along the tilted vertical direction z' from the offset-domain image point $\mathbf{I}_{\mathbf{x_h}}$ to the angle-domain image point $\mathbf{I}_\gamma$.

2. $\mathbf{I}_\gamma$ lies on the normal to the apparent geological dip passing through the crossing point of the source and receiver rays ($\bar{\mathbf{I}}$). $\mathbf{I}_\gamma$ is located at the crossing point of the lines passing through $\mathbf{S_0}$ and $\mathbf{R_0}$ and orthogonal to the source ray and receiver ray, respectively.

3. From the previous geometric results, by invoking Fermat's principle and applying simple trigonometry, we can also easily derive a relationship between the total normal shift $\Delta\mathbf{n}_{\text{tot}} = \left(\mathbf{I}_\gamma - \bar{\mathbf{I}}\right)$ and the total traveltime perturbation caused by velocity errors as follows:

$$\Delta\mathbf{n}_{\text{tot}} = \frac{\Delta t}{2S\cos\gamma}\mathbf{n}, \tag{19}$$

where S is the background slowness around the image point and Δt is defined as the difference between the perturbed traveltime and the background traveltime.

These results are based on the assumption that the velocity is locally smooth in a neighborhood of the imaging point. Furthermore, the relationship expressed in equation (19) depends on the assumption of stationary raypaths, since we need to invoke Fermat's principle. We can assume stationary raypaths if the velocity perturbations are small. Biondi and Symes (2004) discuss these assumptions in details.

The relationship expressed in equation (19) forms the basis of using ADCIGs for MVA. Similar relationships have been extensively used in MVA methods based on constant-offset Kirchhoff migration (Etgen, 1990; Stork, 1992; Meng et al., 1999a,b). Equation (19) can be directly used to transform measurements of depth errors in ADCIGs into traveltime perturbations that can be inverted by a ray-based tomographic inversion; or it can be the foundation for the derivation of accurate RMO functions to be applied to measure depth errors in ADCIGs.

Residual moveout in ADCIGs

The inconsistencies between the migrated images at different aperture angles are the primary source of information for velocity updating during Migration Velocity Analysis (MVA). An effective and robust method for measuring inconsistencies between images is to compute first semblance scans as a function of one "residual moveout" (RMO) parameter, and then pick the maxima of the semblance scan. This procedure is most effective when the residual moveout function used for computing the semblance scans closely approximates the true moveouts in the images.

In this section, we focus our attention on the methods that parametrize the RMO function with only one parameter, but more flexible parameterizations are possible. At the limit, the depth errors could be picked for each value of the reflection angles, but the resulting picks are likely to be noisy. Two attractive alternatives to the one-parameter measurements proposed in this section are: the Dif-

ferential Semblance Optimization (DSO) method (Symes and Carazzone, 1991), and the picking of local dips in migrated CIGs (Chauris et al., 2002a,b). Both of these methods aim at preserving the information contained in the full prestack partial images, while avoiding the drawbacks of picking individual traces in the migrated image.

Appendix A presents the derivation of a RMO functions for scanning 3-D ADCIGs. The starting point of our derivation is the 2-D RMO function presented by Biondi and Symes (2004). Its generalization is based on the 3-D geometrical understanding developed in the previous sections, and it leads to the following expression:

$$\Delta\mathbf{n}_{\mathrm{RMO}} = \frac{\rho-1}{\cos\alpha}\frac{\sin^2\gamma}{\left(1-\sin^2\alpha\cos^2(\eta-\phi)-\sin^2\gamma\right)}z_0\,\mathbf{n}, \tag{20}$$

where ρ is the ratio between the true velocity and the migration velocity, z_0 is the migrated depth of the normal incidence event, α is the geological dip, and η is the azimuth angle of the normal to the geological dip (see Figure 13).

Equation (20) is the general expression of the RMO function in 3-D. For flat reflectors (i.e. $\alpha = 0$) equation (20) becomes the much simpler RMO function (Biondi and Symes, 2004) that follows:

$$\Delta\mathbf{n}_{\mathrm{RMO}} = (\rho-1)\tan^2\gamma\, z_0\,\mathbf{n}. \tag{21}$$

It is also easy to verify that when the reflection azimuth is aligned with the geological dip azimuth (i.e. "dip reflection" with $\eta = \phi$), equation (20) simplifies to the following 2-D RMO function:

$$\Delta\mathbf{n}_{\mathrm{2D-RMO}} = \frac{\rho-1}{\cos\alpha_{x'}}\frac{\sin^2\gamma}{\left(\cos^2\alpha_{x'}-\sin^2\gamma\right)}z_0\,\mathbf{n}, \tag{22}$$

with $\alpha_{x'} = \alpha$.

Similarly, when the reflection azimuth is orthogonal to the geological dip (i.e. "strike reflection" with $\eta - \phi = \pm 90°$), equation (20) simplifies into the following expression:

$$\Delta\mathbf{n}_{\mathrm{RMO}} = \frac{\rho-1}{\cos\alpha}\tan^2\gamma\, z_0\,\mathbf{n}. \tag{23}$$

Equation (23) is the RMO function for flat events, [equation (21)], except for the scaling factor of $1/\cos\alpha$ (with $\alpha = \alpha_{y'}$) that takes into account the inclination of the tilted plane in Figure 13.

The special cases of dip-reflections and strike-reflections depend on the orientation of the geological dip relative to the reflection azimuth and not on the data azimuth. They are thus subsurface (wavefields at depth) properties and not surface (recorded data) properties; that is, they depend on the velocity model in the overburden as well as on the relative orientation of the acquisition direction with respect to the geological dips.

Examples of 3-D ADCIGs in presence of velocity errors

To verify the accuracy of our kinematic analysis of 3-D ADCIGs in presence of migration velocity errors, we compare the predictions of our results [equation (19) and equation (20)] with the actual reflector shifts in the angle-domain image cube obtained from a simple synthetic data set. The data set is the same as the one used in the previous section (5 dipping planes immersed in a vertically layered velocity function). We have migrated the data with a velocity function 3% slower than the correct one; that is, the slowness function is scaled by 1.03 at every depth level.

As we have discussed in the previous sections, the azimuth of the reflections ϕ increases as the aperture angle γ increases. Therefore, equation (19) and the RMO function define curved lines that live in a 5-D space. To verify their accuracy in predicting actual reflector movements we display the image cube for the following three pairs of γ and ϕ: ($\gamma = 0°, \phi = 10°$) in Figure 14, ($\gamma = 20°, \phi = 11°$) in Figure 15, and ($\gamma = 30°, \phi = 13°$) in Figure 16. These are the reflections' angles for the steepest (60 degrees dip) reflector when the velocity is correct, consistently with our assumption of unperturbed rays. All these figures display orthogonal sections cut through the image cube at fixed γ and ϕ and function of the physical coordinates z,x, and y. In panels a) the crosshair is centered

at the coordinates predicted using equation (19); whereas in panels b) the crosshair is centered at the coordinates predicted by the 3-D RMO function expressed in equation (20). The numerical values of these coordinates are shown by the numbers at the edges of the black lines that define the crosshair.

The predictions corresponding to equation (19) were computed starting from a numerical ray-tracing of the reflected events using the correct velocity. The traveltime perturbation Δt was then computed by integrating the slowness perturbations along the unperturbed rays. Given Δt, $\Delta \mathbf{n}_{\text{tot}}$ was computed using equation (19). If the background velocity were constant (straight rays) the procedure outlined above would result in image-point shifts exactly equal to the image-point shifts computed using equation (20). In our example the background velocity increases with depth and therefore the two predictions differ for large aperture angles.

The crosshair in the panels on the left accurately tracks the reflector movements in the corresponding image cubes. These panels demonstrate that equation (19) accurately predicts the actual movements of the reflector across the whole range of aperture angles, even if the reflector analyzed is steeply dipping at 60 degrees.

As expected, the predictions computed by applying equation (20) (panels b) are not as accurate as the predictions computed using equation (19) (panels b). Consistently to the intended use of RMO functions, the shift at normal incidence ($\gamma = 0°$) was picked from the image, whereas the shifts at $\gamma = 20°$ and at $\gamma = 30°$ were computed using equation (20). The predicted shifts track fairly well the reflector movements in the image up to an aperture angle of 20 degrees (Figure 15b), but the straight-rays approximation underlying our derivation of the 3-D RMO function breaks down when either the source or the receiver rays are close to overturning. As it is easy to verify by simple trigonometry, when $\gamma = 30°$ and $\phi = 13°$ (Figure 16b) the take-off angle at the reflection point is about 81 degrees for one of the two rays. A straight ray propagating at such an oblique angle is a poor approximation

of the true ray that starts with the same take-off angle at the reflection point. The true ray quickly becomes more vertical as it travels toward the surface, and consequently it is much shorter than the straight ray. This break down of the assumptions at the basis of the derivation of the 3-D RMO function, causes the substantial overprediction of the reflector movements observed in Figure 16b.

CONCLUSIONS

We present a new methodology for computing 3-D Angle Domain Common Image Gathers (ADCIGs) from the results of wavefield-continuation migration. The proposed methodology is general and can be applied to the results obtained with any wavefield-continuation migration method, including: downward-continuation shot-profile migration, reverse-time shot-profile migration, source-receiver migration, and plane wave migration. Furthermore, our method can be used to compute ADCIGs before imaging and after imaging. These two kinds of ADCIG are related, though we show that they have a different sensitivity to velocity errors.

We successfully applied the proposed methods to the computation of 3-D ADCIGs from a simple synthetic data set. 3-D ADCIGs represent reflections as a function of the reflection azimuth ϕ, in addition to the aperture angle γ. Whereas reflection azimuth is obviously related to the data azimuth, our synthetic-data example demonstrates that they may differ when velocity variations in the overburden distort the wavefield. In the general case, both γ and ϕ are needed to characterize the events and to use ADCIGs for either amplitude analysis or Migration Velocity Analysis (MVA)

To enable the application of 3-D ADCIGs to MVA, we generalize the kinematic analysis of 2-D ADCIGs in presence of migration-velocity errors (Biondi and Symes, 2004). Our analysis yields a quantitative relationship between depth errors measurable in 3-D ADCIGs and traveltime perturbations caused by velocity errors. This relationship can be directly used in a ray-based MVA procedure.

In this paper, we use it for deriving an approximate 3-D Residual Moveout (RMO) function that predicts reflectors' movement when migration velocity is inaccurate. Our derivation of the 3-D RMO function assumes straight rays.

We confirm the accuracy of our kinematic analysis by comparing the image-point shifts predicted by its results with the actual reflector's shifts in the angle-domain image cube obtained from a 3-D synthetic data set with steeply dipping reflectors and a vertically varying propagation velocity. The proposed 3-D RMO function is accurate for a wide range of dips and aperture angles. However, as expected, when rays are close to overturn the straight-rays approximation is inadequate, and the 3-D RMO function overpredicts the actual reflector's movements.

ACKNOWLEDGMENTS

We would like to thank Sam Gray for useful discussions on ADCIGs and for pointing out to us that a plane-wave interpretation of 3-D ADCIGs would overcome the difficulties encountered by a ray-theoretical one.

We would like to acknowledge the financial support of the Stanford Exploration Project's sponsors.

REFERENCES

Aminzadeh, F., Burkhard, N., Long, J., Kunz, T., and Duclos, P., 1996, Three dimensional SEG/EAGE models - an update: The Leading Edge, **2**, 131–134.

Biondi, B., and Palacharla, G., 1996, 3-D prestack migration of common-azimuth data: Geophysics, **61**, 1822–1832.

Biondi, B., and Sava, P., 1999, Wave-equation migration velocity analysis: 69th Ann. Internat. Meeting, Soc. of Expl. Geophys., Expanded Abstracts, 1723–1726.

Biondi, B., and Shan, G., 2002, Prestack imaging of overturned reflections by reverse time migration: 72nd Ann. Internat. Meeting, Soc. of Expl. Geophys., Expanded Abstracts, 1284–1287.

Biondi, B., and Symes, W. W., 2004, Angle-domain common-image gathers for migration velocity analysis by wavefield-continuation imaging: Geophysics: accepted for publication.

Biondi, B., and Vaillant, L., 2000, 3-D wave-equation prestack imaging under salt: 70th Ann. Internat. Meeting, Soc. of Expl. Geophys., 906–909.

Biondi, B., Tisserant, T., and Symes, W., 2003, Wavefield-continuation angle-domain common-image gathers for migration velocity analysis: 73rd Ann. Internat. Meeting, Soc. of Expl. Geophys., 2104–2107.

Biondi, B., 2003, Equivalence of source-receiver migration and shot-profile migration: Geophysics, **68**, 1340–1347.

Brandsberg-Dahl, S., de Hoop, M., and Ursin, B., 1999, Velocity analysis in the common scattering-angle/azimuth domain: 69th Annual Internat. Mtg., Soc. Expl. Geophys., Expanded Abstracts, 1715–1718.

Brandsberg-Dahl, S., de Hoop, M. V., and Ursin, B., 2003, Focusing in dip and AVA compensation on scattering-angle/azimuth common image gathers: Geophysics, **68**, 232–254.

Chauris, H., Noble, M. S., Lambare, G., and Podvin, P., 2002a, Migration velocity analysis from locally coherent events in 2-D laterally heterogeneous media, Part I: Theoretical aspects: Geophysics, **67**, 1202–1212.

Chauris, H., Noble, M. S., Lambare, G., and Podvin, P., 2002b, Migration velocity analysis from locally coherent events in 2-D laterally heterogeneous media, Part II: Applications on synthetic and real data:, **67**, 1213–1224.

Claerbout, J. F., 1985, Imaging the Earth's Interior: Blackwell Scientific Publications.

Clapp, R., and Biondi, B., 2000, Tau domain migration velocity analysis using angle CRP gathers and geologic constraints: 70th Ann. Internat. Mtg., Soc. Expl. Geophys., 926–929.

Clapp, R. G., 2001, Geologically constrained migration velocity analysis: Ph.D. thesis, Stanford University.

de Bruin, C. G. M., Wapenaar, C. P. A., and Berkhout, A. J., 1990, Angle-dependent reflectivity by means of prestack migration: Geophysics, **55**, 1223–1234.

de Bruin, C., 1992, Linear AVO inversion by prestack depth migration: Ph.D. thesis, Delft University.

Etgen, J., 1990, Residual prestack migration and interval velocity estimation: Ph.D. thesis, Stanford University.

Liu, W., Popovici, A., Bevc, D., and Biondi, B., 2001, 3-D migration velocity analysis for common image gathers in the reflection angle domain: 69th Ann. Internat. Meeting, Soc. of Expl. Geophys., Expanded Abstracts, 885–888.

Meng, Z., Bleistein, N., and Valasek, P., 1999a, 3-D analytical migration velocity analysis, Part II: Velocity gradient estimation: 69th Ann. Internat. Meeting, Soc. of Expl. Geophys., 1731–1734.

Meng, Z., Bleistein, N., and Wyatt, K., 1999b, 3-D analytical migration velocity analysis, Part I: Two-step velocity estimation by reflector-normal update: 69th Ann. Internat. Meeting, Soc. of Expl. Geophys., 1727–1730.

Mosher, C. C., Foster, D. J., and Hassanzadeh, S., 1997, Common angle imaging with offset plane waves: 67th Annual Internat. Mtg., Soc. Expl. Geophys., Expanded Abstracts, 1379–1382.

Mosher, C., Jin, S., and Foster, D., 2001, Migration velocity analysis using common angle image gathers: 71th Ann. Internat. Mtg., Soc. of Expl. Geophys., 889–892.

Ottolini, R., and Claerbout, J. F., 1984, The migration of common-midpoint slant stacks: Geophysics, **49**, 237–249.

Prucha, M., Biondi, B., and Symes, W., 1999, Angle-domain common-image gathers by wave-equation migration: 69th Ann. Internat. Meeting, Soc. Expl. Geophys., Expanded Abstracts, 824–827.

Rickett, J., and Sava, P., 2002, Offset and angle-domain common image-point gathers for shot-profile migration: Geophysics, **67**, 883–889.

Sava, P., and Fomel, S., 2003, Angle-domain common-image gathers by wavefield continuation methods: Geophysics, **68**, 1065–1074.

Schultz, P. S., and Claerbout, J. F., 1978, Velocity estimation and downward-continuation by wavefront synthesis: Geophysics, **43**, 691–714.

Stolk, C. C., and Symes, W. W., 2004, Kinematic artifacts in prestack depth migration: Geophysics, **69**, 562–575.

Stork, C., 1992, Reflection tomography in the postmigrated domain: Geophysics, **57**, 680–692.

Symes, W. W., and Carazzone, J. J., 1991, Velocity inversion by differential semblance optimization: Geophysics, **56**, 654–663.

Wapenaar, C. P. A., and Berkhout, A. J., 1987, Full prestack versus shot record migration: 69th Ann. Internat. Meeting, Soc. of Expl. Geophys., Expanded Abstracts, Session:S15.7.

Xie, X. B., and Wu, R. S., 2002, Extracting angle domain information from migrated wavefield: 72th Ann. Internat. Mtg., Soc. Expl. Geophys., 1360–1363.

Xu, S., Chauris, H., Lambare, G., and Noble, M. S., 2001, Common-angle migration: A strategy for imaging complex media: Geophysics, **66**, 1877–1894.

APPENDIX A

In this Appendix we derive the expression for the residual moveout (RMO) function to be applied to 3-D ADCIGs computed by wavefield continuation.

We start from the 2-D expression for RMO, as derived by Biondi and Symes (2004):

$$\Delta\mathbf{n}_{\mathrm{2D-RMO}} = \frac{\rho-1}{\cos\alpha_{x'}}\frac{\sin^2\gamma}{\left(\cos^2\alpha_{x'}-\sin^2\gamma\right)}z_0\,\mathbf{n}, \tag{A-1}$$

In 3-D, this relationship is valid on the tilted plane shown Figure 3, where the migrated depth of the normal incidence event z_0 is now the depth along the tilted plane z_0'. Therefore, the migrated depth z_0 needs to be scaled by a factor of $1/\cos\alpha_{y'}$, where $\alpha_{y'}$ is the inclination of the tilted plane. In 3-D equation (A-1) becomes:

$$\begin{aligned}\Delta\mathbf{n}_{\mathrm{RMO}} = & \\ & \frac{\rho-1}{\cos\alpha_{x'}}\frac{\sin^2\gamma}{\left(\cos^2\alpha_{x'}-\sin^2\gamma\right)}z_0'\,\mathbf{n} = \\ & \frac{\rho-1}{\cos\alpha_{x}\cos\alpha_{y}}\frac{\sin^2\gamma}{\left(\cos^2\alpha_{x'}-\sin^2\gamma\right)}z_0\,\mathbf{n}.\end{aligned} \tag{A-2}$$

When $\alpha_{x'}$ and $\alpha_{y'}$ are available, the RMO function could be directly evaluated using the expression in equation (A-2). However, in several situations it is more useful to express the RMO function

explicitly as a function of the geological dip α, the azimuth angle of the normal to the geological dip η, and the azimuth angle of the reflected event ϕ (see Figure **??**). To derive the desired expression, we use the following two trigonometric relationships among the angles:

$$\cos\alpha = \cos\alpha_{x'}\cos\alpha_{y'}, \qquad \text{and} \qquad \sin\alpha_{x'} = \sin\alpha\cos(\eta-\phi). \tag{A-3}$$

Substituting equations (A-3) into equation (A-2), we obtain the following final result:

$$\Delta\mathbf{n}_{\mathrm{RMO}} = \frac{\rho-1}{\cos\alpha}\frac{\sin^2\gamma}{\left(1-\sin^2\alpha\cos^2(\eta-\phi)-\sin^2\gamma\right)}z_0\,\mathbf{n}. \tag{A-4}$$

LIST OF FIGURES

1 Illustration of the method for computing ADCIGs before imaging. Orthogonal slices of the prestack wavefield after downward continuation with the correct velocity to the depth of 700 meters; that is, the depth of the flat reflector: zero-offset section (panel a), and the common-midpoint gather at 1,410 meters (panel b). Panel c) shows the complete (i.e. for all depths) ADCIG at 1,410 meters.

2 A schematic of the geometry of an ADCIG gather in 2-D. Depending on the context, the angles can be either the angles formed by the propagation direction of the rays, or those formed by the propagation direction of the associated plane waves. The arrows indicate positive angles; that is, β_s, β_r, and α_x are negative and γ is positive. This sign convention is consistent with upward propagating rays (plane waves).

3 A schematic of the geometry of an ADCIG gather in 3-D. The geometry is analogous to the 2-D case illustrated in Figure 2. In contrast with the schematic of Figure 2, the plane of coplanarity is not vertical but it is tilted by $\alpha_y{}'$ and rotated by ϕ with respect to the horizontal coordinates. Notice also that the angles $\delta_{s'}$ and $\delta_{r'}$ formed by the rays (plane waves) propagation directions with the "true" vertical axis are different from the angles $\beta_{s'}$ and $\beta_{r'}$ formed by the rays with the tilted vertical axis.

4 ODCIG (panel a) and ADCIG(γ) (panel b) after migration with the correct velocity. This CIGs are taken from the same data and at the same surface location as the ADCIG shown in Figure 1c.

5 Depth slice (z=580 meters) of the migrated image of the SEG-EAGE salt data set. The crosshair is centered at a horizontal location where the top of the salt dips at approximately 50 degrees in the cross-line direction.

6 ADCIG computed using the approximate 2-D relationship (panel a), and ADCIG computed using the correct 3-D relationship (panel b). The aperture angle γ of the top of the salt reflection ($z \simeq$

600 meters) is overestimated in panel (a), whereas the bottom of the salt reflection ($z \simeq 2{,}100$ meters) is the same in the two panels.

7 Reflectors' geometry for the synthetic data set used to illustrated 3-D ADCIGs. The reflectors are slanted planes, dipping at 0°, 15°, 30°, 45° and 60° toward increasing x and y; they are oriented with an azimuth of 45° with respect to the in-line direction.

8 ADCIGs as functions of depth (z) and aperture angle (γ) for two different reflection azimuths and at constant horizontal location ($x = y = 450$ meters): $\phi = 10°$ (a), and $\phi = 15°$ (b).

9 ADCIG as a function of aperture angle (γ) and reflection azimuth (ϕ) at constant depth ($z = 1{,}430$ meters) and horizontal location ($x = y = 450$ meters).

10 ADCIGs as functions of depth (z) and reflection azimuth (ϕ) for three different aperture angles and at constant horizontal location ($x = y = 450$ meters): $\gamma = 4°$ (a), $\gamma = 20°$ (b), and $\gamma = 30°$ (c).

11 Illustration of the sensitivity to velocity errors of the ADCIGs computed before imaging. The panels are the same as in Figure 1; that is, they display orthogonal slices of the prestack wavefield after downward continuation to the depth of 700 meters, but the velocity used for downward continuation was 10% higher than the correct one. Panel a) displays the zero-offset section, panel b) displays the common-midpoint gather at 1,410 meters, and panel c) shows the complete (i.e. for all depths) ADCIG at 1,410 meters.

12 Illustration of the sensitivity of ADCIGs computed after imaging to velocity errors. The panels are the same as in Figure 4, but after migration with a velocity 10% higher than the correct one. Panel a) displays the ODCIG and panel b) the ADCIG(γ). Notice that the range of γ increases from Figure 4b to Figure 12b.

13 Geometry of an ADCIG for a single event migrated with the wrong velocity. The transformation to the angle domain shifts the offset-domain image point $\mathbf{I}_{\mathbf{x_h}}$ to the angle-domain image point

$\mathbf{I}_\gamma$. Both image points lie on the tilted plane of coplanarity.

14 Orthogonal sections cut through the migrated image cube obtained with a velocity function too low by 3%. The image cube is at fixed $\gamma = 0°$ and $\phi = 10°$. In panel a), the crosshair is centered at the coordinates predicted for the 60 degrees reflector by using equation (19) and the traveltime perturbations computed along the the true raypaths. In panel b), the reflector's coordinates are predicted by using the 3-D RMO equation in (20).

15 Orthogonal sections cut through the migrated image cube obtained with a velocity function too low by 3%. The image cube is at fixed $\gamma = 20°$ and $\phi = 11°$. In panel a), the crosshair is centered at the coordinates predicted for the 60 degrees reflector by using equation (19) and the traveltime perturbations computed along the the true raypaths. In panel b), the reflector's coordinates are predicted by using the 3-D RMO equation in (20).

16 Orthogonal sections cut through the migrated image cube obtained with a velocity function too low by 3%. The image cube is at fixed $\gamma = 30°$ and $\phi = 13°$, In panel a), the crosshair is centered at the coordinates predicted for the 60 degrees reflector by using equation (19) and the traveltime perturbations computed along the the true raypaths. In panel b), the reflector's coordinates are predicted by using the 3-D RMO equation in (20).

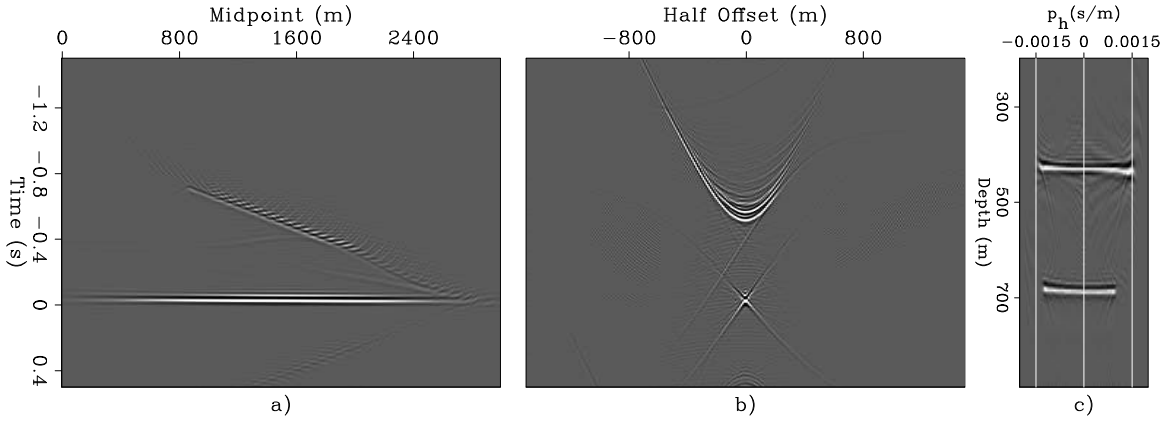
Midpoint (m)
0
800
1600
2400
Time (s)
−1.2
−0.8
−0.4
0
0.4
a)
Half Offset (m)
−800
0
800
b)
p_h(s/m)
−0.0015
0
0.0015
Depth (m)
300
500
700
c)

Figure 1.

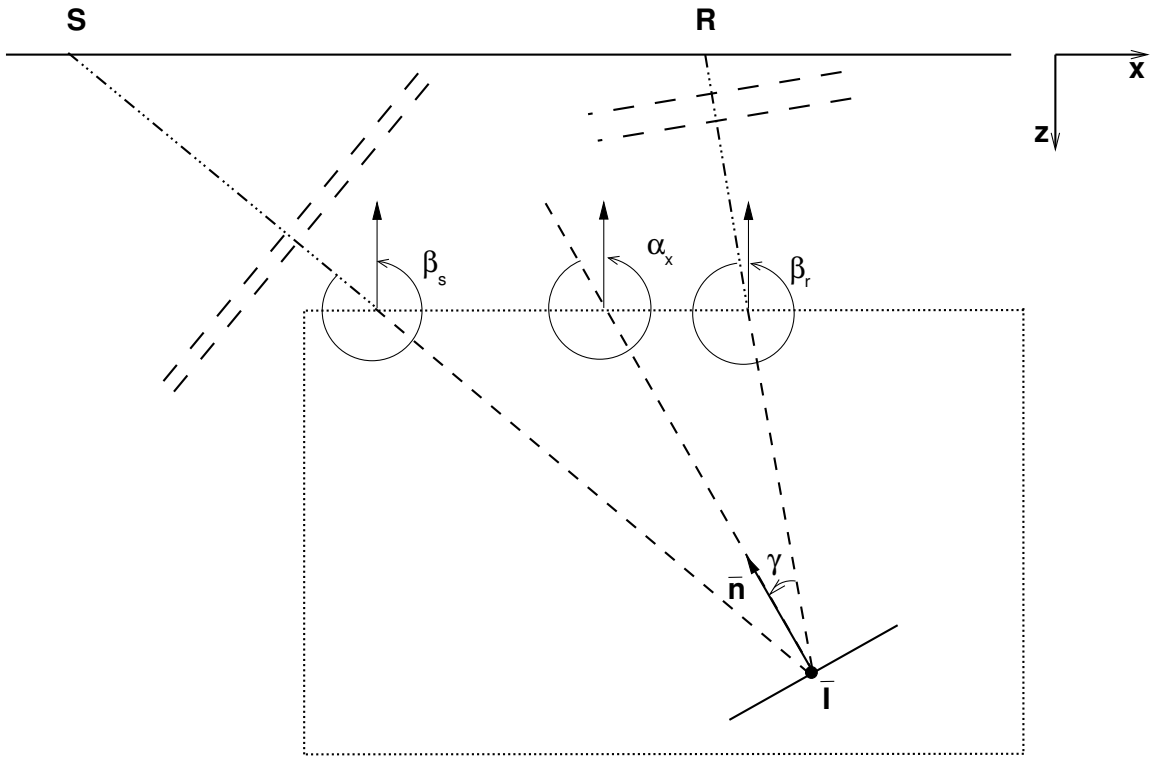

Figure 2.

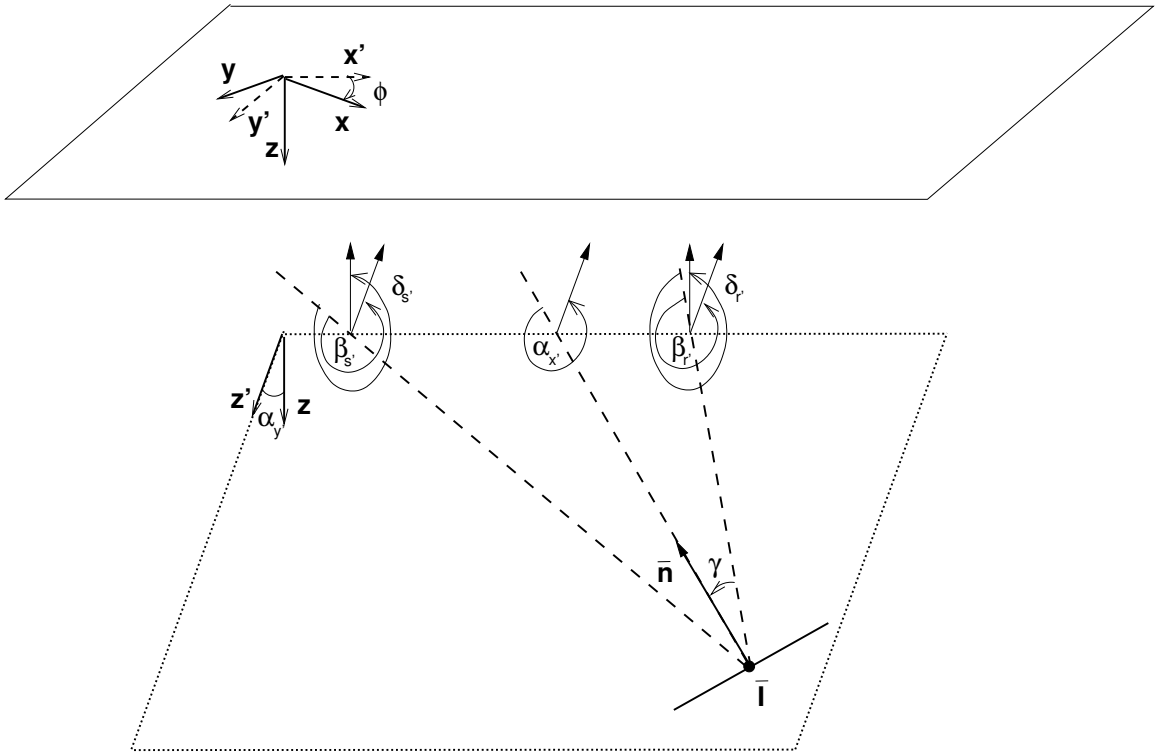

Figure 3.

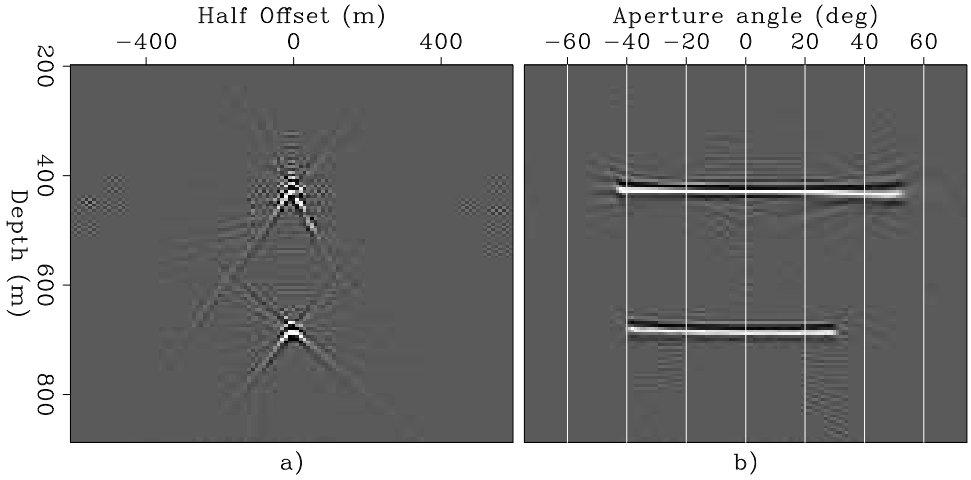
Half Offset (m)
−400
0
400
Aperture angle (deg)
−60 −40 −20 0 20 40 60
Depth (m)
200
400
600
800
a)
b)

Figure 4.

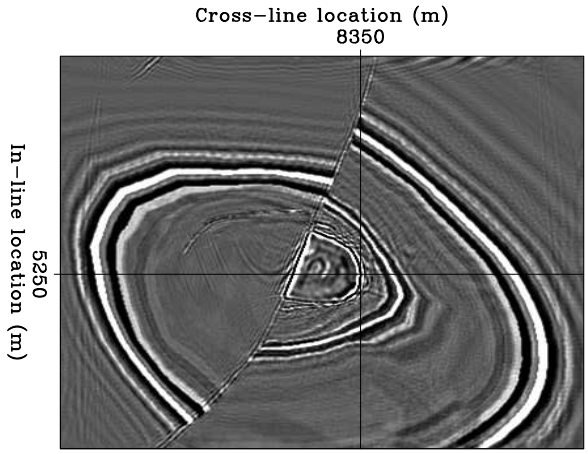

Figure 5.

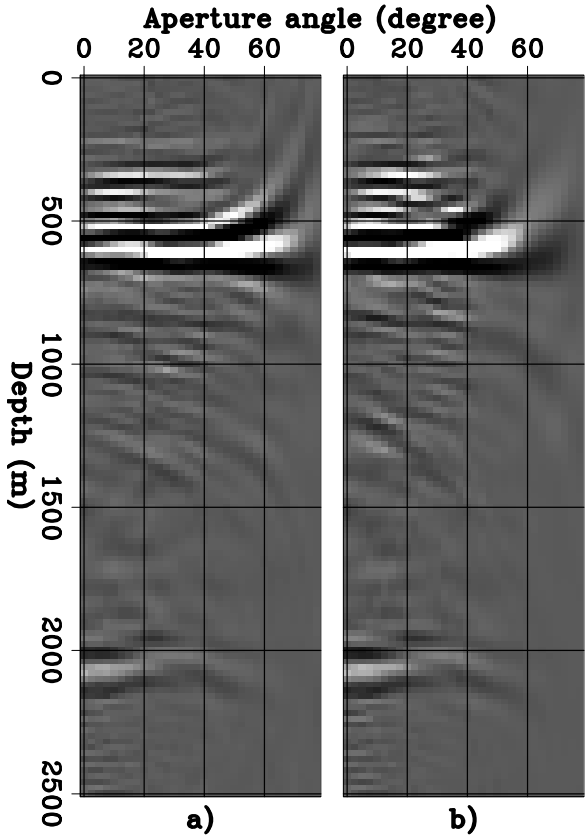
Aperture angle (degree)
0 20 40 60
0 20 40 60
Depth (m)
0
500
1000
1500
2000
2500
a)
b)

Figure 6.

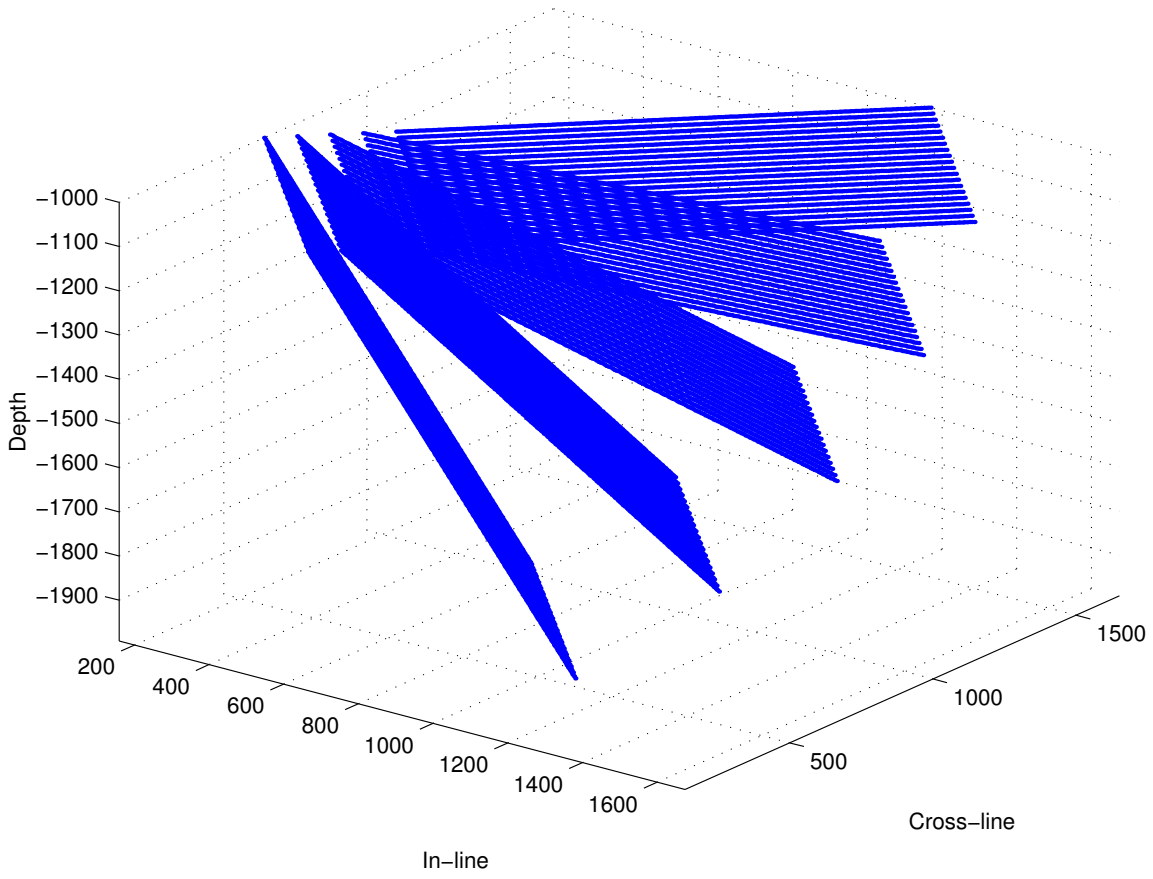
−1000
−1100
−1200
−1300
−1400
−1500
−1600
−1700
−1800
−1900
Depth
200
400
600
800
1000
1200
1400
1600
In−line
500
1000
1500
Cross−line

Figure 7.

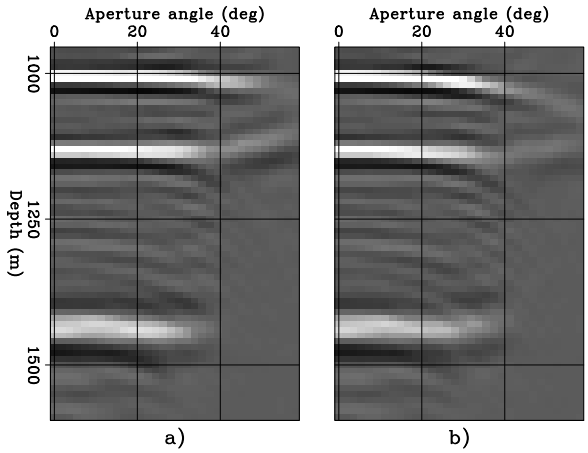
Aperture angle (deg)
0
20
40
1000
1250
1500
Depth (m)
a)
Aperture angle (deg)
0
20
40
b)

Figure 8.

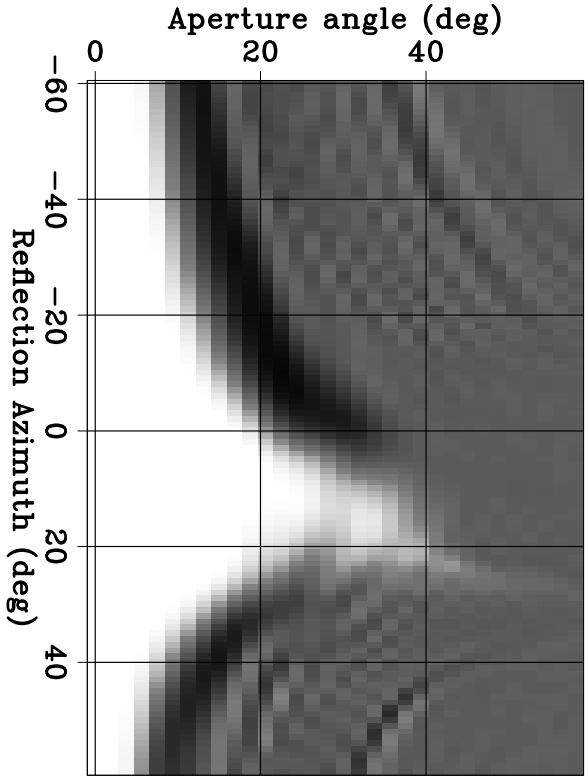
Aperture angle (deg)
0
20
40
Reflection Azimuth (deg)
−60
−40
−20
0
20
40

Figure 9.

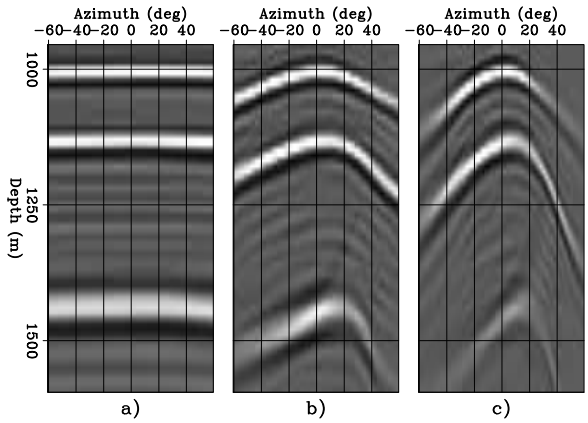
Azimuth (deg)
−60−40−20 0 20 40
Azimuth (deg)
−60−40−20 0 20 40
Azimuth (deg)
−60−40−20 0 20 40
1000
1250
1500
Depth (m)
a)
b)
c)

Figure 10.

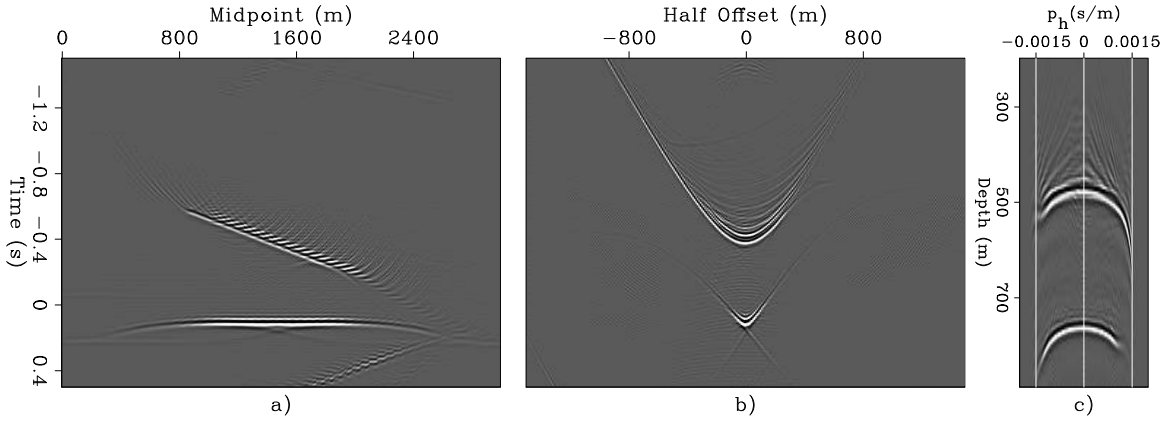
Midpoint (m)
0
800
1600
2400
Time (s)
−1.2
−0.8
−0.4
0
0.4
a)
Half Offset (m)
−800
0
800
b)
p_h(s/m)
−0.0015
0
0.0015
Depth (m)
300
500
700
c)

Figure 11.

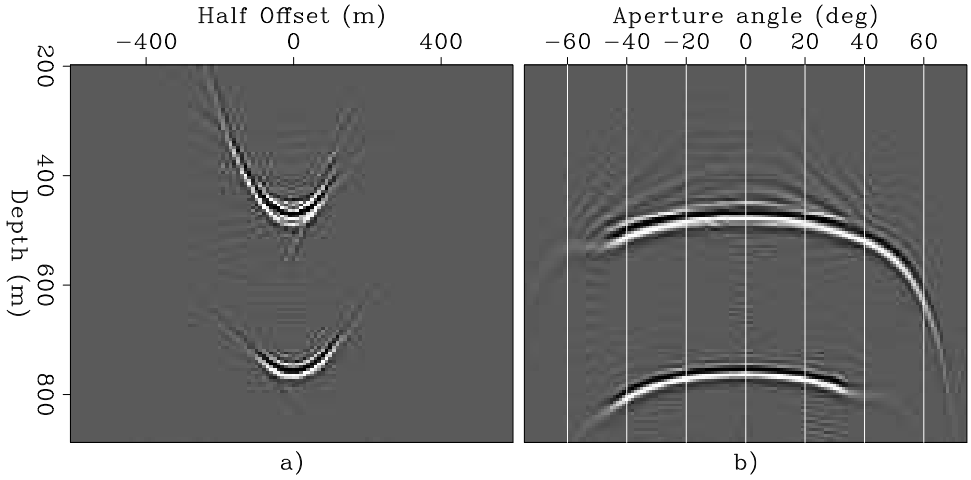
Half Offset (m)
−400
0
400
Aperture angle (deg)
−60 −40 −20 0 20 40 60
Depth (m)
200
400
600
800
a)
b)

Figure 12.

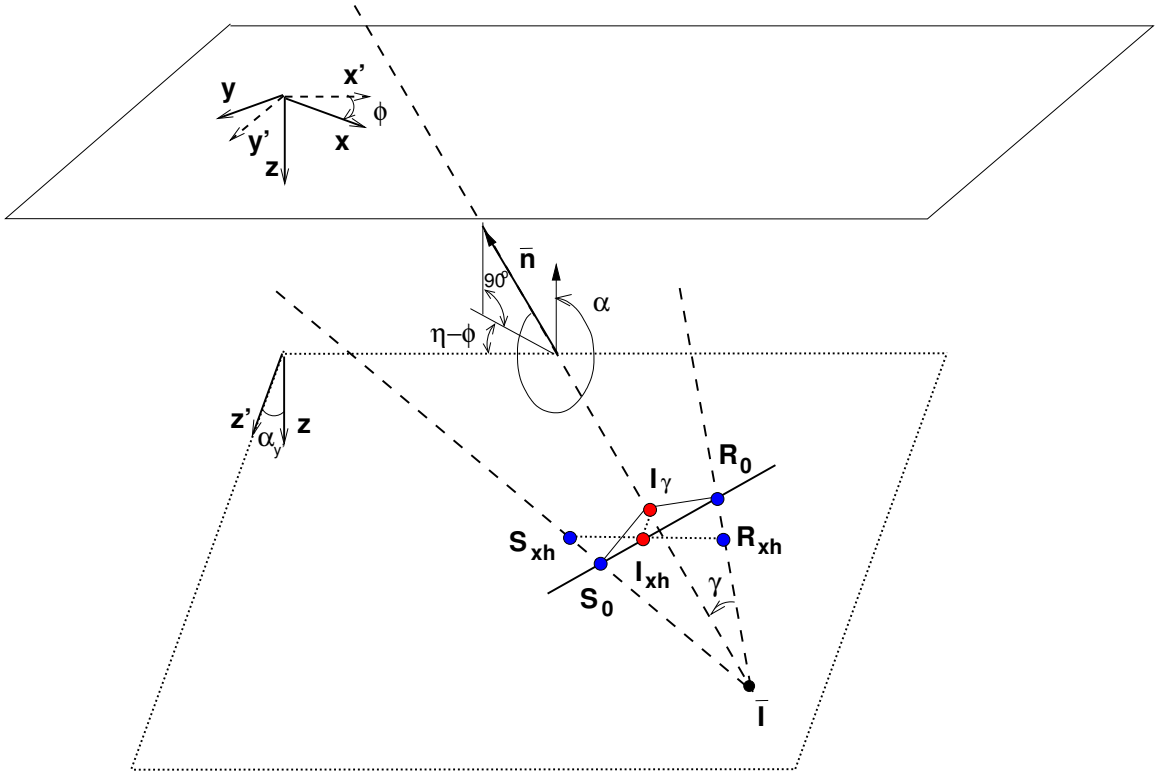

Figure 13.

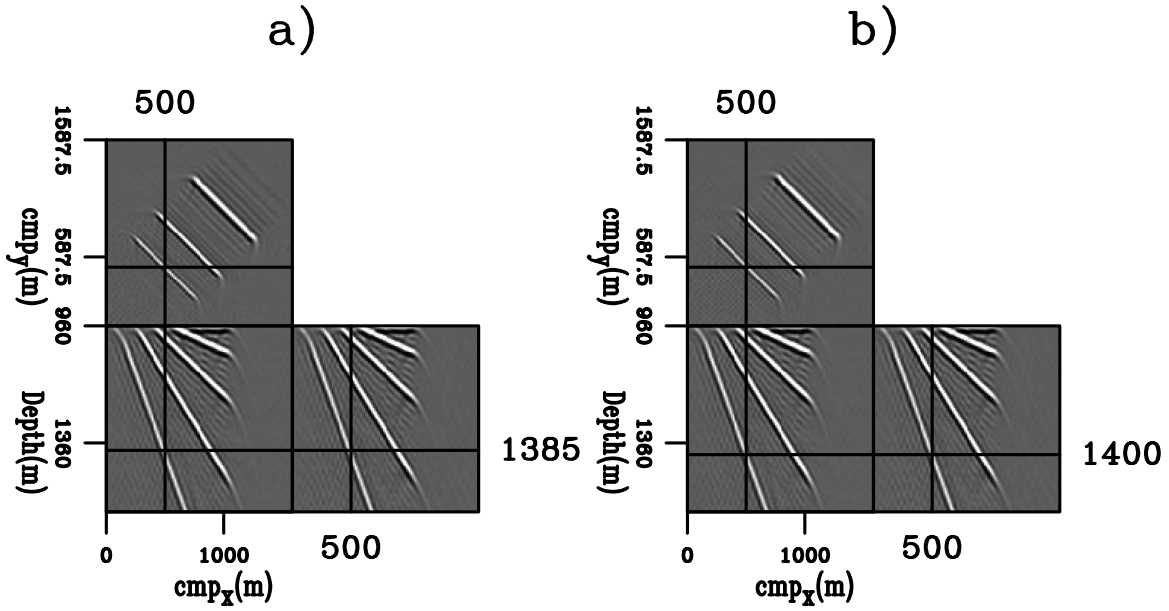
a)
b)
500
1587.5
587.5
960
1360
cmp$_Y$(m)
Depth(m)
1385
1400
0
1000
500
cmp$_X$(m)

Figure 14.

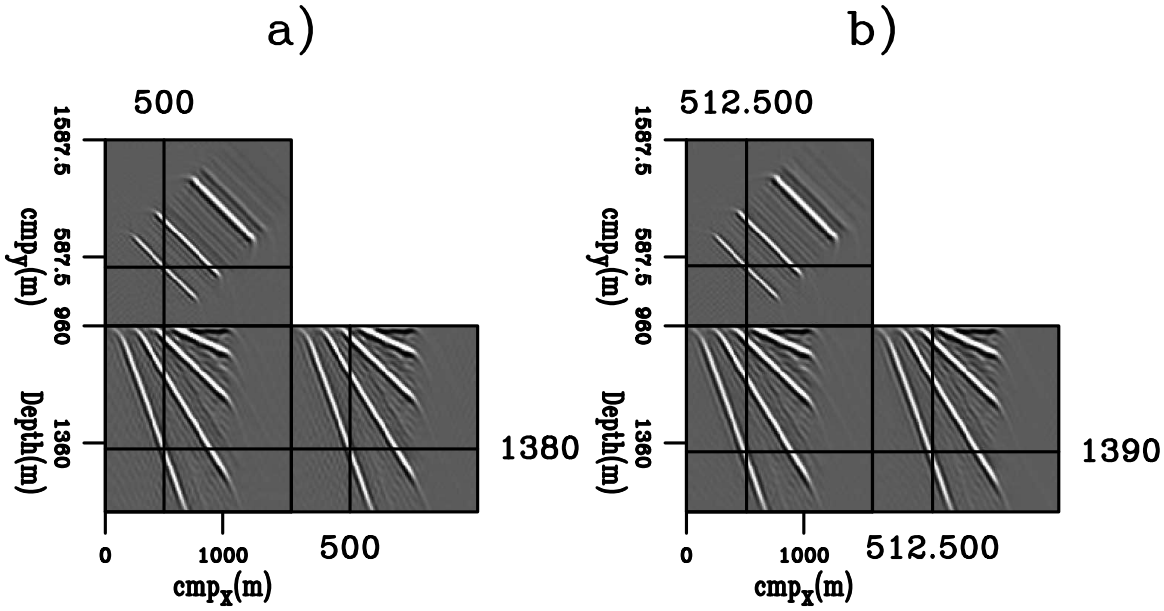
a)
b)
500
512.500
1587.5
587.5
960
1360
cmp$_Y$(m)
Depth(m)
1380
1390
0
1000
500
512.500
cmp$_X$(m)

Figure 15.

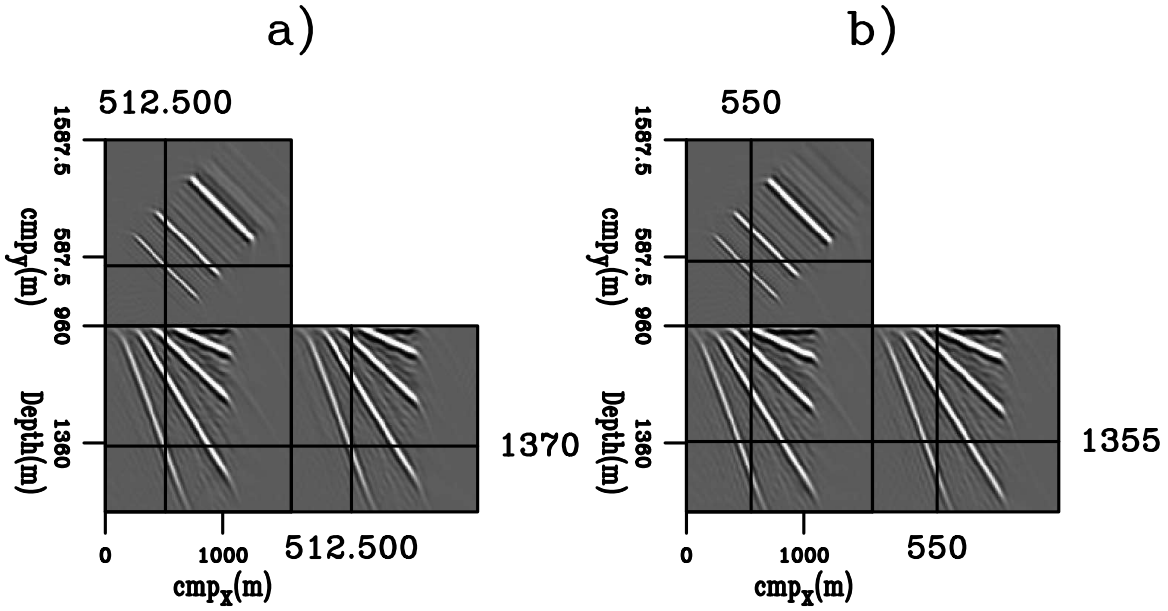
a)
512.500
1587.5
587.5
960
1360
cmpY(m)
Depth(m)
1370
0
1000
512.500
cmpX(m)
b)
550
1587.5
587.5
960
1360
cmpY(m)
Depth(m)
1355
0
1000
550
cmpX(m)

Figure 16.